Reversible shear-induced crystallization above equilibrium freezing temperature in a lyotropic surfactant system

Vikram Rathee[a], Rema Krishnaswamy[b], Antara Pal[c], V. A. Raghunathan[c], Marianne Impéror-Clerc[d], Brigitte Pansu[d], and A. K. Sood[a,b,1]

[a]Department of Physics, Indian Institute of Science, Bangalore 560012, India; [b]Jawaharlal Nehru Centre for Advanced Scientific Research, Jakkur, Bangalore 560064, India; [c]Raman Research Institute, Bangalore 560080, India; and [d]Laboratoire de Physique des Solides, Unité Mixte de Recherche 8502 Centre National de la Recherche Scientifique, Université Paris-Sud 11, 91405 Orsay Cedex, France

Edited by Noel A. Clark, University of Colorado Boulder, Boulder, CO, and approved August 2, 2013 (received for review March 18, 2013)

We demonstrate a unique shear-induced crystallization phenomenon above the equilibrium freezing temperature (T_K^o) in weakly swollen isotropic (L_i) and lamellar (L_α) mesophases with bilayers formed in a cationic-anionic mixed surfactant system. Synchrotron rheological X-ray diffraction study reveals the crystallization transition to be reversible under shear (i.e., on stopping the shear, the nonequilibrium crystalline phase L_c melts back to the equilibrium mesophase). This is different from the shear-driven crystallization below T_K^o, which is irreversible. Rheological optical observations show that the growth of the crystalline phase occurs through a preordering of the L_i phase to an L_α phase induced by shear flow, before the nucleation of the L_c phase. Shear diagram of the L_i phase constructed in the parameter space of shear rate ($\dot{\gamma}$) vs. temperature exhibits $L_i \rightarrow L_c$ and $L_i \rightarrow L_\alpha$ transitions above the equilibrium crystallization temperature (T_K^o), in addition to the irreversible shear-driven nucleation of L_c in the L_i phase below T_K^o. In addition to revealing a unique class of nonequilibrium phase transition, the present study urges a unique approach toward understanding shear-induced phenomena in concentrated mesophases of mixed amphiphilic systems.

shear-induced phase separation | strongly binding counterions | coagels

Shear is known to assist crystallization below the equilibrium freezing temperature in complex fluids like colloidal glasses (1, 2), dense granular suspensions (3), polymer melts (4, 5), micellar solutions of block copolymers (6), and multicomponent surfactant systems (7, 8). Shear-driven crystallization is equally relevant for simple fluids like bulk metallic glasses (9), molecular liquids (10), and atomic systems (11). The general understanding is that shear lowers the energy barrier for nucleation and accelerates the growth of a stable crystalline phase from a metastable, amorphous/isotropic solution at Peclet number $\mathrm{Pe} = \frac{\sigma a^3}{k_B T} > 1$, where σ is the shear stress, a is the characteristic length scale, and $k_B T$ is the thermal energy (12). The crystalline phase primarily induced by the effect of flow on the internal structure and ordering of the constituents does not revert to the starting fluid state when the imposed shear is removed, indicating that the phenomenon is not a dynamic phase transition. In the present study, we report a unique phenomenon, where under steady shear, crystallization occurs above the equilibrium crystallization temperature (T_K^o) in an isotropic mesophase (L_i) consisting of bilayers formed in a lyotropic surfactant system. Notably, above T_K^o, when the imposed shear is removed, the crystalline phase melts back to the starting L_i phase.

The studies were carried out in a cationic-anionic mixed surfactant system formed by SDS and the strong binding counter-ion paratoluene hydrochloride (PTHC) in water. At equilibrium, the organic counter-ion PTHC has the tendency to remain at the micelle–water interface, decreasing the spontaneous curvature of the micellar aggregates and transforming them from cylinders to bilayers (13, 14). The equilibrium phase behavior of the concentrated phases was investigated recently in this system, and a novel isotropic phase (L_i) of bilayers was reported (15). The L_i phase with short-range translational correlations occurs when the quasi–long-range positional order of the L_α phase is destroyed at higher temperatures or at higher concentrations of counter-ions through the creation of defects in the bilayer. Further, it was proposed that the optically isotropic L_i phase is made up of bilayers with pores/randomly connected passages. Importantly, this phase was reported to exhibit flow birefringence, suggesting that the symmetry of the phase can be broken by shear. Here, we report from in situ synchrotron rheological X-ray scattering measurements and rheological optical studies in the L_i and L_α phases of a lyotropic mixed surfactant system, a unique shear-induced phase transition to a crystalline phase above the equilibrium freezing temperature, which is reversible under shear. We construct a shear diagram (Fig. 1) in the parameter space of shear rate and temperature, which reveals, in addition to crystallization (region III, Fig. 1), the observation of an $L_i \rightarrow L_\alpha$ transition (region II, Fig. 1) in a concentrated isotropic mesophase above a low critical shear rate of 0.05 s^{-1}. In Fig. 1, (R) and (IR) are used to emphasize the reversible nature and irreversible nature of the phases, respectively, on stopping the shear. The high-resolution powder X-ray diffraction data obtained for the nonequilibrium $L_c(R)$ phases in region III were indexed to a triclinic lattice (Figs. 2 and 3). By following the growth kinetics, we show that the crystalline phase nucleates in the shear-induced L_α phase (Fig. 4), with a higher concentration of the organic counter-ions compared with the starting L_i phase at rest. Consequently, we propose that the driving mechanism for the formation of the $L_c(R)$ phase is the shear-induced redistribution of the hydrophobic counter-ions in the bilayers of the L_α phase.

The proposed mechanism is very different from the shear-reversible crystallization reported in colloidal hard sphere fluids (16) in a large-amplitude oscillatory shear (LAOS) at Pe > 1, where the shear-induced ordering is determined by the balance between Brownian forces and the interparticle interactions, with the range of interaction set by the applied strain amplitude. So far, shear-induced phase transitions reported in bilayer-forming amphiphilic systems have shown that an isotropic sponge phase (L_3) of interconnecting bilayers can transform to a lamellar

Author contributions: V.R., R.K., V.A.R., and A.K.S. designed research; V.R., R.K., A.P., M.I.-C., and B.P. performed research; V.R. and R.K. analyzed data; R.K., M.I.-C., and B.P. proposed and carried out rheological SAXS (Rheo-SAXS) measurements at Soleil, France; V.R. and A.P. carried out Rheo-SAXS measurements at Soleil, France; and V.R., R.K., and A.K.S. wrote the paper.

The authors declare no conflict of interest.

This article is a PNAS Direct Submission.

[1]To whom correspondence should be addressed. E-mail: asood@physics.iisc.ernet.in.

This article contains supporting information online at www.pnas.org/lookup/suppl/doi:10.1073/pnas.1304777110/-/DCSupplemental.

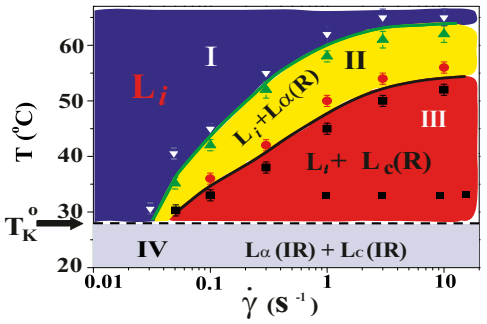

Fig. 1. Shear diagram for the isotropic phase (L_i). Region III (shaded in red) demonstrates the coexistence of L_i with the shear-induced crystalline phase ($L_c(R)$). Coexistence of the L_i and $L_\alpha(R)$ phases is observed in region II (shaded in yellow). The crystalline ($L_c(IR)$) and lamellar ($L_\alpha(IR)$) phases nucleate irreversibly in the L_i phase under shear (region IV, shaded in blue) below T_K^o. Only the transitions above T_K^o (indicated by the dashed line) are reversible under shear. The approximate boundaries demarcating different regions are shown by solid lines. The data points corresponding to the final phases, constructed from the stress relaxation measurements, are shown by different symbols indicating L_i (inverted white triangles), $L_\alpha(R)+L_i$ (green triangles and red circles), and $L_c(R)+L_i$ (black squares).

phase (L_α) consisting of a stack of bilayers with 1D quasi–long-range positional order (17) or that a dilute L_α phase is shear-transformed to a collapsed surfactant-rich L_α phase with very little water between the bilayers, coexisting with excess solvent (18). In this context, the studies have been restricted to the swollen L_α or L_3 phase with highly flexible bilayers dominated by steric repulsion, where the transitions occur due to shear-induced suppression of thermal fluctuations above a critical shear rate of $\dot{\gamma}_c$ (19). Because $\dot{\gamma}_c \sim \phi^n$, where ϕ is the surfactant volume fraction and the exponent n lies (18) in the range of 1.5–3, the transitions are absent for $\phi > 0.3$ within the experimentally accessible range of shear rates (~1,000 s^{-1}) (20). Our present study is different from the earlier studies on sponge phases because it examines the role of steady shear in weakly swollen, concentrated ($\phi > 0.5$) isotropic phases (15, 21) in driving a nonequilibrium transition from isotropic $L_i \rightarrow L_\alpha(R)/L_c(R)$ at Pe $\ll 1$. The structural transition is feasible through a shear-induced segregation/microphase separation of the hydrophobic counterions in bilayers to tune the spontaneous curvature at the bilayer–water interface. Counter-ion redistribution under shear is equally relevant for different classes of mixed amphiphilic systems, where shear drives a change in microstructure of the micellar aggregates transforming them from cylinders into bilayers (22, 23), or vice versa (24, 25), in a flow field or shear promotes the formation of pores in vesicles (26) through the partial segregation of amphiphiles in the bilayers. A microphase separation driven by shear flow can manifest in concentrated mesophases as shear-induced phase transitions, a possibility that, to our knowledge, was completely unexplored until the present work.

Results and Discussion

Shear Diagram of the L_i Phase. All rheological measurements (unless otherwise stated) were carried out on the L_i phase prepared at a composition C_{start}, where the PTHC-to-SDS molar ratio (α) is 1.5 and the overall surfactant weight fraction (ϕ) is 0.4. Our studies clearly established that at rest or at low shear rates, the crystalline phase (L_c) could be obtained by cooling the L_i phase below 14 °C. On heating, the L_c phase melts at 28 °C, which is identified as the equilibrium freezing temperature or Krafft temperature (T_K^o). Because the L_i phase can be supercooled down to 14 °C, it explains the absence of the L_c phase in the equilibrium phase diagram of the study by Pal et al. (15). The attractive interactions giving rise to a weakly swollen behavior result in the coexistence of the L_i phase with excess solvent, which is a characteristic feature of a class of amphiphilic systems that form coacervate phases (21). To study shear-induced nonequilibrium phenomena in such systems, it is reasonable to isolate them from the excess solvent (more details on the sample composition and equilibrium phase behavior are provided in *SI Appendix*, *SI Text*, Figs. S1 and S2, and Tables S1 and S2). The main result of our study is the nonequilibrium phase behavior of the L_i phase summarized in Fig. 1, obtained by combining polarizing optical microscopy with stress relaxation measurements. To construct the shear diagram (Fig. 1) reproducibly, the following protocol was established. The vial containing the sample prepared at the composition C_{start} was placed in a water bath at a fixed temperature T, and the phase-separated L_i was loaded into the cone-plate geometry at the same temperature. The sample compositions at rest for the phase-separated L_i have been determined at three different temperatures (*SI Appendix*, Fig. S1 and Table S1). Each data point in the shear diagram was constructed by carrying out stress relaxation measurements at a fixed shear rate (with a waiting time of 1 s for each data point). The above protocol was repeated for many different temperatures. The notable features of the shear diagram ($\dot{\gamma}$ vs. T) are the $L_i+L_c(R)$ (region III) (see Movie S1), and $L_i+L_\alpha(R)$ (region

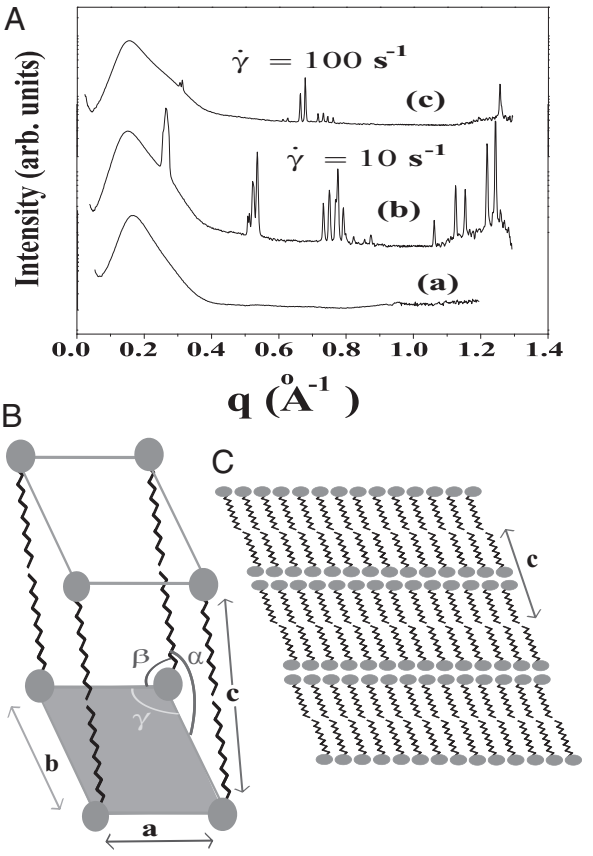

Fig. 2. X-ray diffraction pattern of the equilibrium L_i phase (corresponding to region I, Fig. 1) and shear-induced crystalline ($L_c(R)$) phases (corresponding to region III, Fig. 1). (*A*) Diffraction pattern from the L_i phase at rest at $T = 33$ °C is shown in curve a; Rheo-SAXS data in the radial geometry obtained at $T = 33$ °C indicate the coexistence of the L_i and $L_c(R)$ phases for samples sheared at (*i*) 10 s^{-1} in curve b and (*ii*) 100 s^{-1} in curve c. arb., arbitrary. There is a shift in peak positions and relative intensities of the Bragg peaks in curve c with respect to curve b indicates a change in the structure of $L_c(R)$ with the shear rate. A triclinic unit cell (*B*) and a schematic sketch of the proposed crystalline structure (*C*) are illustrated.

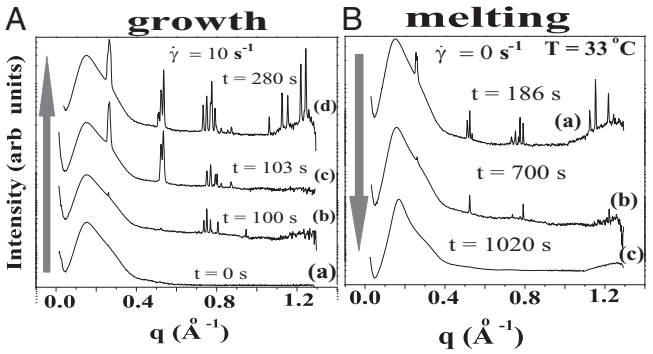

Fig. 3. Time-resolved Rheo-SAXS data of the L_i phase (corresponding to region III, Fig. 1) in the radial geometry at $T = 33$ °C indicates growth of the $L_c(R)$ phase with time, at 10 s^{-1}, in which the times shown correspond to that from the start of shear (*A*) and melting of the $L_c(R)$ phase at 33 °C on stopping the shear, in which the times shown correspond to that from the stoppage of shear (*B*).

II) transitions occurring well above T_K^o. The $L_i \rightarrow L_\alpha(R)$ transition observed in region II is shear-reversible (Movie S2), and the textures observed under shear confirm that the transition to the $L_\alpha(R)$ phase is not accompanied by the formation of onions. Region IV shows the shear-irreversible $L_i \rightarrow L_\alpha(IR) + L_c(IR)$ transition below T_K^o, to form a gel consisting of a percolating network of plate-like crystals with solvent trapped in the interstitial regions, known as a coagel phase (27). In region III, the optical micrographs confirm the appearance of an oily streak texture corresponding to the $L_\alpha(R)$ phase (Fig. 4*A*), accompanied by a sharp increase in viscosity in stress relaxation measurements (Fig. 4*C*) and the subsequent growth of crystallites of $L_c(R)$ in $L_\alpha(R)$ (Fig. 4*B*). The criterion for reaching the steady state is that at a given temperature and shear rate, within the maximum time over which the samples have been sheared, which is 20,000 s (~6 h), the shear-induced phases identified from the optical texture do not evolve any further. However, any further evolution of viscosity and the crystallite size with time, under shear, are not taken into account when constructing the shear diagram. For shear rates <0.1 s^{-1}, the data points (Fig. 1) at boundaries I and II between the L_i and $L_\alpha(R)$ phases and at boundaries II and III between the $L_\alpha(R)$ and $L_c(R)$ phases were obtained by shearing the samples for 40,000 s (12 h). The solid line demarcating regions II and III in Fig. 1, where the $L_c(R)$ phase melts, indicates a positive shift in the Krafft temperature under shear. A similar shear diagram constructed by means of a parallel-plate geometry is given in *SI Appendix*, Fig. S3. Because the main focus of the present study is the crystallization observed above T_K^o, all the results outlined in the remaining sections below will pertain to region III of Fig. 1.

Structure of L_c (*R*) Phases. Rheological small angle x-ray scattering (Rheo-SAXS) measurements were carried out at 33 °C ($>T_K^o$, corresponding to region III in Fig. 1) to determine the structure of the shear-induced crystalline phases. At zero shear, the diffraction pattern of the L_i phase, which consists of a broad peak (Fig. 2*A*, curve a) with an average d-spacing of 41.0 Å, fitted well to the model for the L_α phase (15). The model parameters (*SI Appendix*, Table S2) indicate that the number of correlated bilayers is ~2 for the L_i phase compared with ~13 in the weakly swollen L_α phase of the same system. On shearing the L_i phase at 33 °C (which is significantly much above T_K^o) at a shear rate ($\dot{\gamma}$) of 10 s^{-1}, sharp crystalline peaks appear in the small- and wide-angle regions, coexisting with the broad peak corresponding to the L_i phase (Fig. 2*A*, curve b and Fig. 3*A*, curves b–d). Because the crystals that form are likely to be oriented along flow, the time-resolved structures of the crystallites are obtained from the analysis of diffraction data obtained in a radial geometry that gives a powder pattern (*SI Appendix*, Fig. S8*A*). The diffraction peaks obtained after a shearing time of $t = 100$ s (Fig. 3*A*, curve b) were indexed to a triclinic structure (Fig. 2*B*) with lattice parameters of $a = 8.4$ Å, $b = 8.8$ Å, and $c = 24.4$ Å and $\alpha = 96.0°$, $\beta = 91°$, and $\gamma = 102°$, with a unit cell volume of 1,758 Å^3. Interestingly, the crystalline peak positions, as well as their relative intensities, are seen to evolve under shear. The subsequent diffraction peaks obtained at $t = 103$ s (Fig. 3*A*, curve c) were indexed to a triclinic structure (Fig. 2*B*) with lattice parameters $a = 9.7$ Å, $b = 12.8$ Å, and $c = 24.4$ Å and $\alpha = 79.0°$, $\beta = 79°$, and $\gamma = 89°$ with a unit cell volume of 2,942 Å^3. The crystalline peaks (Fig. 3*A*, curve d) obtained after 280 s (when a final steady state with no further temporal evolution of the peak positions or relative intensities is reached) were indexed to a triclinic structure with lattice parameters $a = 13.3$ Å, $b = 16.6$ Å, and $c = 25.2$ Å and $\alpha = 101.0°$, $\beta = 100°$, and $\gamma = 107°$, with a corresponding unit cell volume of 5,087 Å^3 (*SI Appendix*, Fig. S5 and Table S3). Hence, under shear with time, although the crystal lattice remains the same, the unit cell volume increases by increasing the area of the *a*–*b* plane, keeping the length of the *c* axis nearly constant. The sharp peaks in the wide-angle region (Fig. 2*A*) confirm that the alkyl chains of SDS are in a crystalline state and the proposed crystalline phase consists of bilayers (Fig. 2*C*), with the bilayer thickness (corresponding to lattice parameter *c*) determined by the tilt of crystalline alkyl chains of SDS molecules and the lattice parameters *a* and *b* determined by the in-plane ordering, as well as the tilt of the chains, as proposed in SDS crystal phases (28). We surmise that a shear-driven increase in the number of surfactant molecules forming the basis of the triclinic lattice and the resulting change in the packing of the chains in the unit cell can give rise to the observed shift in peak positions and relative intensities with time. Accordingly, the significant increase in the lattice parameters *a* and *b* corresponding to the bilayer plane suggests a change in the composition (α)

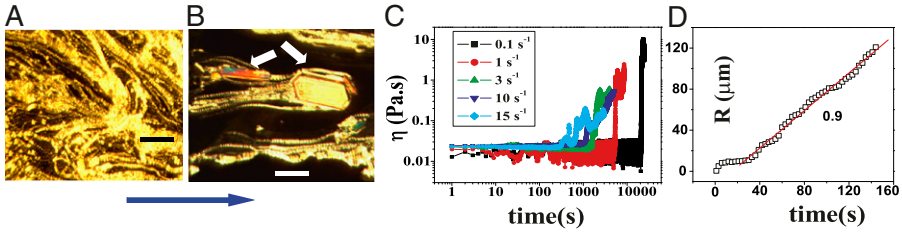

Fig. 4. Stress relaxation and rheological optical measurements in the L_i phase. Polarizing optical micrographs at different times after the onset of shear at $\dot{\gamma} = 10$ s^{-1}, $T = 33$ °C, shows the growth of shear-induced $L_\alpha(R)$ identified from the oily streak texture in the L_i phase (indicated by the dark optically isotropic background) (*A*); growth of birefringent crystallites [$L_c(R)$, indicated by arrows] in the L_α phase (*B*) (Scale bars in *A* and *B*, 200 microns); viscosity (η) as a function of time (*t*) at different shear rates ($\dot{\gamma}$) measured in a cone-plate geometry, $T = 33$ °C (*C*); and increase in the radius R of the crystal with time, under conditions as described in the main text (*D*).

of the bilayers through incorporation of additional surfactant molecules and para toluidine hydrogen cations (PTH^+) in the unit cell. At a shear rate of 10 s^{-1}, the structure of the $L_c(R)$ phase in the nonequilibrium steady state is the same as the equilibrium L_c phase (*SI Appendix*, Fig. S7). The coexistence of L_i and L_c (R) phases was also observed at $\dot{\gamma} = 100$ s^{-1} (Fig. 2*A*, curve c). Interestingly, there is a significant shift in positions of the Bragg peaks compared with the peak positions at lower shear rates (Fig. 2*A*, curve b), indicating a variance in the structure of $L_c(R)$. The crystalline peaks were indexed again to a triclinic structure with different lattice parameters, where a = 11.6 Å, b = 20.5 Å, and c = 20.9 Å and $\alpha = 93°$, $\beta = 99°$, and $\gamma = 102°$, with a unit cell volume of 4,795 $Å^3$.

Nucleation, Growth, and Melting of L_c (R) Phases. In situ synchrotron X-ray scattering, which is a powerful probe to resolve growth kinetics under shear, can give a reliable time scale for the onset of crystallization. In Rheo-SAXS measurements, the data acquisition was started at the onset of shear. At $\dot{\gamma} = 10$ s^{-1}, the growth of the crystallite occurs after 100 s. The temporal evolution of the crystal volume [which is proportional to the integrated intensity $Q(t)$ estimated from the first-order crystalline peak at q = 0.263 $Å^{-1}$ as described in *SI Appendix*, Fig. S9] is given by $V_c(t) \sim t^3$, suggesting that the growth law for the present system is similar to that seen during the crystal growth from a melt in hard sphere colloidal suspensions (29, 30). However, we admit that caution should be exercised when interpreting these results obtained by assuming a powder diffraction pattern from randomly oriented crystals. A partial alignment of the crystallites can occur due to the growth of $L_c(R)$ in an aligned $L_\alpha(R)$ phase (evident in the diffraction patterns obtained in the tangential geometry at a time t = 134 s during the early stages of growth; *SI Appendix*, Fig. S8*B*), as well as from the time-dependent orientation of crystallites in the direction of flow. Nevertheless, from polarizing microscopy experiments (Fig. 4*D*), we have verified the linear growth law for the crystal size where the average radius of the crystallite $R \sim t$ (here, the time t is measured after the crystallite has grown to a size of 5 μm in a steady shear of 10 s^{-1}) by monitoring the growth of a crystallite in an oscillatory shear (as soon as the steady shear is stopped, a strain amplitude γ = 10 at an angular frequency ω = 1 rad/s is applied to achieve strain rate amplitude $\gamma\ \omega$ of 10 s^{-1}). It is interesting that the growth kinetics in the present system follow the Wilson–Frenkel model, which proposes that the growth rate is determined by the rate of adsorption of molecules at the crystal interface. As evident from Fig. 3*B*, on stopping the shear, the intensity of the crystalline peaks decreases gradually with time due to the melting of the $L_c(R)$ phase. The melting of the crystalline mass with time follows a sigmoidal curve of the functional form $Q(t) = I_2 + \frac{I_1 - I_2}{1 + (t/t_o)^p}$ (*SI Appendix*, Fig. S9). After 1,000 s, only the broad peak from the L_i phase remains (Fig. 3*B*, curve c) confirming that the $L_c(R)$ phase observed above T_K^o is an out-of-equilibrium phase, occurring only when an external shear field is imposed.

An important finding from the rheological optical measurements that gives further insight into the crystallization phenomenon is that the nucleation of the $L_c(R)$ phase occurs in a shear-induced lamellar phase (Fig. 4 *A* and *B*). In Rheo-SAXS measurements, the partial alignment of the crystallites along the direction of flow (evident in the first-order crystalline peaks) in the tangential configuration at the early stages of growth (*SI Appendix*, Fig. S8*B*) is consistent with the alignment of bilayers of $L_\alpha(R)$ along the walls of the Couette and the growth of crystallites in $L_\alpha(R)$. X-ray diffraction peaks of $L_\alpha(R)$ are not evident in Rheo-SAXS measurements when the $L_\alpha(R)$ peaks overlap with L_i. This has been established by shearing the L_i phase below T_K^o, where the final state after stopping the shear corresponds to the $L_\alpha(IR)$ phase coexisting with $L_c(IR)$ (*SI Appendix*, Fig. S7). Fig. 4*C* shows the viscosity (η) as a function of time (t) at different shear rates at 33 °C measured in a cone-plate geometry. At $\dot{\gamma} = 1$ s^{-1}, although η at the onset of shear remains constant at 20 mPa/s, after shearing for ∼5,000 s (defined as a delay time t_p), viscosity increases by two orders of magnitude accompanied by birefringent oily streaks corresponding to a lamellar texture as seen from the polarizing optical micrographs (Fig. 4*A*). Further shearing leads to the growth of birefringent crystallites only in the $L_\alpha(R)$ phase (Fig. 4*B*), reaching a final steady state with the coexistence of L_i and $L_c(R)$ phases (Movie S1 *A* and *B*). On stopping the shear, the crystallites melt and the starting L_i phase is recovered (Movie S1*C*). It is seen that at a fixed shear rate and temperature, the delay time t_p, which marks the incubation time for the onset of crystallization (identified from the sharp increase in viscosity as well as the optical micrographs), varies (*SI Appendix*, Figs. S10 and S11) as expected for a nucleation process (17). However, the onset of crystallization appears to require a minimum strain ($\gamma = \dot{\gamma}.t$) of 1,000, which is also consistent with the Rheo-SAXS data (Fig. 3*A*, curve b). Note that the shear-induced crystallization observed presently at $\gamma > 1{,}000$ should be contrasted with colloidal hard sphere fluids, where the phenomenon is absent under steady shear (16, 31). We further confirm that the $L_i \rightarrow L_c(R)$ or $L_i \rightarrow L_\alpha(R)$ transition does not occur under oscillatory shear up to a strain amplitude of 10. This behavior is very different from colloidal systems (31) or block copolymers (32), where the phase transition occurs only due to a shear-induced ordering under LAOS.

Shear-Reversible Crystallization in a Weakly Swollen L_α Phase Above T_K^o. Having established that the growth of the $L_c(R)$ phase occurs only in the shear-induced $L_\alpha(R)$ phase, it is important to verify whether $L_c(R)$ phases can also be induced by shearing an equilibrium L_α phase. We now show that a shear-reversible crystallization is also obtained in the L_α phase of the same system prepared at a different sample composition (α = 1, ϕ = 0.5). Here, the L_α phase, which coexists with excess solvent (15), consists of a turbid dispersion of multilamellar vesicles (MLVs), as confirmed from polarizing microscopy observations. The diffraction pattern obtained from the L_α phase at rest at 33 °C shows a lamellar peak at 43.7 Å (Fig. 5, curve a). Only one diffraction peak is measured for the L_α phase because the structure factor reaches the asymptotic value of 1 near the second-order peak. However, the second-order lamellar peak is present at lower temperatures (*SI Appendix*, Fig. S2). X-ray diffraction patterns of the L_α phase sheared at 30 s^{-1} reveal a lamellar peak with d-spacing of 40.1 Å, in addition to sharp crystalline peaks in the small- and wide-angle regions (Fig. 5, curve b) that were indexed to

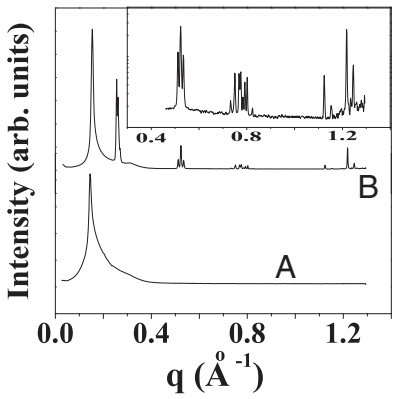

Fig. 5. Tangential diffraction patterns obtained in Rheo-SAXS measurements of the L_α phase prepared at α = 1, ϕ = 0.5 at 33 °C: $\dot{\gamma} = 0$ s^{-1} (*A*) and $\dot{\gamma} = 30$ s^{-1} (*B*).

a triclinic lattice (*SI Appendix*, Fig. S6 and Table S4) with the same structure and lattice parameters as the equilibrium L_c phase. Another feature evident in the Rheo-SAXS experiments on the L_α phase is the decrease of d-spacing under shear accompanied by a decrease in the width and increase in height of the lamellar Bragg peak, indicating an increased correlation between the bilayers. This decrease in d-spacing under shear in concentrated lamellar phases with MLVs can arise when the water can permeate across the bilayers of the vesicle to fill the interstitial volume, thus lowering the packing constraints under shear (33).

Proposed Mechanism for Shear-Reversible Crystallization. Because the $L_c(R)$ phase always nucleates in a nonequilibrium L_α phase, we propose below a possible mechanism for the crystallization that occurs in two steps. In the first step, at a strain >1,000, the randomly connected bilayers of the L_i phase align along the direction of shear to form the L_α phase. We speculate that one possible pathway for this transition in the concentrated phase presently studied is through the disruption of bilayer passages by unbinding and redistributing the hydrophobic counter-ions. We further suggest that crystallization occurs in the second step, when the bilayers permeable to solvent under shear can get stretched, with the large deformation increasing the effective area of the bilayers, and hence the dynamic surface tension. The surface tension can be lowered by the absorption of hydrophobic counter-ions (which have a preference for the micelle–water interface) into the bilayers, from the solvent or through the redistribution of counter-ions within the bilayers between the stretched and unstretched regions. The crystalline phase is likely to nucleate in the L_α bilayers with a larger concentration of PTH^+ ions. In our study, we have further provided direct experimental evidence through elemental analysis (*SI Appendix*, *SI Text*) for the increase in the concentration of the hydrophobic PTH^+ counter-ions in the shear-induced crystalline phase $L_c(R)$. At 33 °C, the α value of the L_i phase at rest is 1.5. However, the measured α for $L_c(R)$ phases is always greater than 2 and the same as that in the supercooled L_i (*SI Appendix*, Table S1) phase, where the growth of the $L_c(IR)$ phase occurs under shear. It is noteworthy in this context that the $L_c(R)$ and $L_c(IR)$ phases have the same triclinic structure with identical lattice parameters. The evolution of the crystal structure under shear (Fig. 3*A*), as discussed earlier, also supports the proposed change in composition of the bilayers under shear. In addition, the linear growth law (Fig. 4*D* and *SI Appendix*, Fig. S9) lends additional support to the proposed mechanism, indicating that the crystal growth kinetics are determined by the adsorption of PTH^+ ions at the $L_c(R)$ - L_i interface. Moreover, a shear-induced crystallization through a change in composition of the bilayers, where the crystalline phase can nucleate only in bilayers with $\alpha > 2$, can further explain the absence of a single-phase region for $L_c(R)$ in the shear diagram (Fig. 1).

The proposed mechanism involves both a change in spontaneous curvature as well as the stretching of bilayers under shear. In ionic surfactant systems with oppositely charged strong binding counter-ions (22–24), when the shear effect on the aggregate structure was taken into account in the deformation energy of a free bilayer (25) through a shear-dependent contribution of spontaneous curvature C_o arising from unbinding of counter-ions, the resultant shear diagram obtained by minimizing the free energy could predict a shear-induced vesicle-to-micelle transition. Similarly, in mixed lipid/surfactant systems, shear-induced partial segregation within the bilayer of the initially evenly distributed amphiphiles is believed to give rise to a change in spontaneous curvature and the membrane line tension leading to pore formation (26). Our study suggests that an analogous phenomenon of shear-induced modification of spontaneous curvature can drive phase transitions in concentrated bilayer-forming mesophases. It is also worthwhile to note that shear-induced stretching in MLVs (34), which are highly permeable to water, leads to formation of entangled tubular vesicles at low shear rates, with applied strain being the control parameter for the onset of transition. The strain value of ~1,000 for the vesicle-to-tubule transition is comparable to that required for the onset of crystallization in the system under study.

In the equilibrium phase diagram of the SDS/PTHC/water system, because T_K^o of the L_c phase increases with α (*SI Appendix*, Fig. S13), the increase in the melting point of the crystalline phase with the shear rate as evident in the shear diagrams of the L_i phase (Fig. 1) is likely to arise from a shear rate-dependent increase in α of the $L_c(R)$ phase. The $\dot{\gamma}$ -dependent shift in the composition of the shear-induced phase is also consistent with the different lattice parameters obtained for L_c(R) phases formed at different shear rates (Fig. 2*A*, curves b and c). It should also be noted, however, that the transitions occur only for shear rates in the range of 0.05–100 s^{-1}. It is important to note that the $L_i \rightarrow L_c(R)/L_\alpha(R)$ transitions discussed in the present study also occur when the L_i phase is sheared in the presence of excess solvent, indicating that the solvent phase does not contribute to the transition (*SI Appendix*, Fig. S12). Shear-reversible crystallization above T_K^o was also observed for single-phase samples of L_i (Movie S3).

Conclusions and Perspectives

To summarize, we have shown a unique shear-reversible, first-order transition from an isotropic phase to crystalline/lamellar phases in a mixed amphiphilic system. The occurrence of these transitions in the highly concentrated mesophases (with $\phi > 0.5$) above a low critical shear rate (~0.05 s^{-1}) suggests that the mechanism driving the shear-induced transitions in the present system with a limited swelling behavior should be very different from that of the swollen lamellar or sponge phase. Because the L_i phase under study is proposed to form through the proliferation of dislocations in the L_α phase (15), it is relevant in this context to address the role of the imposed shear field in suppressing the dislocations, thus stabilizing the L_α phase. It is worthwhile to mention here that earlier studies on the effect of shear on dislocation loops have yielded conflicting results near the smectic-A/nematic transition (35, 36). By following the kinetics of nucleation under shear, we also show that an $L_\alpha(R)$ phase forms as a pretransition before the onset of crystallization. This is not surprising, considering that the L_c phase has a lamellar structure with crystalline alkyl chains. This is similar to the appearance of the 1D phase as a precursor for the 3D shear-induced crystalline phase, which has been observed, for instance, in the form of string-like structures in dense colloidal suspensions (31, 37) or a smectic phase in melts of flexible polymers (5).

In the context of multicomponent surfactant systems, understanding the role of lamellar ordering induced by shear will be an important step toward controlling the microstructure of the different shear-induced crystalline structures in coagel phases. Although the kinetics of lamellar-to-coagel transitions have been studied under static conditions, there are relatively few reports of these studies under shear. In the shear diagram (Fig. 1, region IV) presented in our study, we further show that the final shear-thickened state obtained from the starting L_i phase consists of the coagel phase below T_K^o, whereas the percolating network of crystalline platelets is absent above T_K^o, although the crystal structures are identical at $\dot{\gamma} = 10$ s^{-1}. This suggests that formation of coagel phases proceeds in two stages, where shear promotes the formation of L_α in the first stage, and subsequently the nucleation of crystalline platelets, and in the second stage, the platelets percolate to form a 3D network above a critical volume fraction of the crystallites. In industrial manufacturing processes, mixing (shear) is an important control parameter because it homogenizes multicomponent systems as well as enhancing the kinetics of crystallization. The present finding may be of interest

to the food processing industry, where the solidification of edible fats and oils is essential when manufacturing margarine, reduced fat spreads, ice cream, chocolate (38), and honey (39), or in consumer industry when manufacturing bar soaps, personal care creams, toothpastes, and lubricant greases (40).

Another outcome of the present study is the possible role of shear-induced phase segregation of amphiphiles within the bilayers in driving the crystallization. The role of microphase separation driven by shear flow in concentrated mesophases has not been incorporated in any of the theoretical models for nonequilibrium phase transitions in bilayer-forming amphiphilic systems comprising surfactants, block copolymers, and microemulsions. Understanding shear as a strategy to control the spontaneous curvature of bilayers of mixed amphiphilic systems is also expected to have significant applications in the design of novel drug delivery systems (41), controlling the permeability of bilayers in onion phases used for encapsulation, in addition to tuning the viscosity during flow processing of surfactant-based products in consumer industry.

Materials and Methods

Ternary solutions of SDS and PTHC (purchased from Sigma-Aldrich and used without further purification) at the desired molar ratio $\left(\alpha = \frac{[PTHC]}{[SDS]}\right)$ of the two components and at the total surfactant weight fraction $\left(\phi = \frac{SDS+PTHC}{SDS+PTHC+water}\right)$ were prepared in deionized water. Rheological measurements were carried out on samples prepared at (*i*) $\alpha = 1.5$, $\phi = 0.4$ and (*ii*) $\alpha = 1$, $\phi = 0.5$. Rheo-SAXS measurements were performed at the SWING beamline of the SOLEIL synchrotron (Proposal 20110293) using a fixed energy of 15 keV and a sample-to-detector distance of 898.42 mm. An MCR-501 rheometer (Anton Paar) equipped with a Couette cell (with a rotating inner cylinder and a temperature-controlled static outer cylinder, gap = 0.2 mm) was mounted on the SAXS beamline (42). The 2D scattering patterns with the X-ray beam parallel or perpendicular to the flow direction (tangential or radial geometry) were recorded on an AVIEX CCD camera formed by four detectors, and appropriate corrections were applied to the data (*SI Appendix*, Fig. S4).

The shear diagram (Fig. 1) was constructed through polarizing optical microscopy measurements in a stress-controlled rheometer (MCR 102; Anton Paar) with a temperature-controlled cone-plate geometry (cone diameter = 25 mm, cone angle = 2°). Preshearing was avoided when loading the samples, and a humidity chamber was used to prevent evaporation of solvent. Images were recorded on an eight-bit color CCD camera (0.75C, 1,200 × 980 pixels; Lumenera) fitted with a microscope objective (20×/0.28 N.A.; Mitutoyo).

ACKNOWLEDGMENTS. We acknowledge SOLEIL (Gif-sur-Yvette, France) for provision of synchrotron radiation facilities, and we thank Florian Meneau for assistance in using beamline SWING. We thank M. Mani for technical assistance with shear cells and Santosh Prasad Gupta for preliminary Rheo-SAXS experiments in the laboratory. A.K.S. thanks the Council for Scientific and Industrial Research (CSIR) for research support through the Bhatnagar Fellowship. R.K. thanks the Department of Science and Technology (DST) for the Ramanujan Fellowship. V.R. thanks the CSIR for the Senior Research Fellowship and DST for travel support for Rheo-SAXS experiments at SOLEIL.

1. Shereda LT, Larson RG, Solomon MJ (2010) Boundary-driven colloidal crystallization in simple shear flow. *Phys Rev Lett* 105(22):228302–228305.
2. Wu YL, Derks D, van Blaaderen A, Imhof A (2009) Melting and crystallization of colloidal hard-sphere suspensions under shear. *Proc Natl Acad Sci USA* 106(26): 10564–10569.
3. Tsai JC, Voth GA, Gollub JP (2003) Internal granular dynamics, shear-induced crystallization, and compaction steps. *Phys Rev Lett* 91(6):064301–064304.
4. Li L, Lambreva D, de Jeu WH (2004) Lamellar ordering and crystallization in a symmetric block copolymer. *J Macromol Sci, Chem* B43(1):59–70.
5. Li L, de Jeu WH (2004) Shear-induced smectic ordering in the melt of isotactic polypropylene. *Phys Rev Lett* 92:075506–075509.
6. Phoon CL, Higgins JS, Allegra G, van Leeuwen P, Staples E (1993) Shear induced crystallization and melting of a micellar solution. *Proc R Soc Lond A Math Phys Sci* 442: 221–230.
7. Mazzanti G, Guthrie SE, Marangoni AG, Idziak SHJ (2007) A conceptual model for shear-induced phase behavior in crystallizing cocoa butter. *Crystal Growth and Design* 7:1230–1241.
8. Mazzanti G, Marangoni AG, Idziak SHJ (2005) Modeling phase transitions during the crystallization of a multicomponent fat under shear. *Phys Rev E Stat Nonlin Soft Matter Phys* 71(4 Pt 1):041607–041618.
9. Lohwongwatana B, Schroers J, Johnson WL (2006) Strain rate induced crystallization in bulk metallic glass-forming liquid. *Phys Rev Lett* 96(7):075503–075506.
10. Gray RA, Warren PB, Chynoweth S, Michopoulos Y, Pawley GS (1995) Crystallization of molecular liquids through shear-induced nucleation. *Proc R Soc Lond A Math Phys Sci* 448:113–120.
11. Heyes DM (1986) Shear thinning and thickening of the Lennard-Jones liquid. A molecular dynamics study. *J Chem Soc Faraday Trans 2* 82:1365–1383.
12. Onuki A (1997) Phase transitions of fluids in shear flow. *J Phys Condens Matter* 9: 6119–6157.
13. Hassan PA, Raghavan SR, Kaler EW (2002) Microstructural changes in SDS micelles induced by hydrotropic salt. *Langmuir* 18:2543–2548.
14. Ghosh SK, Rathee V, Krishnaswamy R, Raghunathan VA, Sood AK (2009) Re-entrant phase behavior of a concentrated anionic surfactant system with strongly binding counterions. *Langmuir* 25(15):8497–8506.
15. Pal A, Pabst G, Raghunathan VA (2012) Defect-mediated lamellar-isotropic transition of amphiphilic bilayers. *Soft Matter* 8:9069–9072.
16. Ackerson BJ, Pusey PN (1988) Shear-induced order in suspensions of hard spheres. *Phys Rev Lett* 61:1033–1036.
17. Leon E, Bonn D, Meunier J, Al-Kahwaji A, Kellay H (2001) Shear-induced first-order sponge-to-lamellar transition in a lyotropic surfactant system. *Phys Rev Lett* 86: 938–941.
18. Porcar L, Hamilton WA, Butler PD (2003) Scaling of structural response of L_3 sponge phases in the "sweetened" cetylpyridinium/hexanol/dextrose/brine system. *Langmuir* 19(26):10779–10794.
19. Cates ME, Milner ST (1989) Role of shear in the isotropic-to-lamellar transition. *Phys Rev Lett* 62(16):1856–1859.
20. Kleman M (1999) The lamellar and sponge phases of dilute surfactant systems: Structures and defects at equilibrium and under shear. *Pramana - Journal of Physics* 53:107–119.
21. Pal A, Bharath P, Dastidar SG, Raghunathan VA (2012) Collapse and coacervation of a lamellar phase by inter-headgroup bridging. *Soft Matter* 8:927–930.
22. Danino D, Talmon Y, Zana R (2000) Cryo-TEM of thread-like micelles: On-the-grid microstructural transformations induced during specimen preparation. *Colloids Surf A Physicochem Eng Asp* 169:67–73.
23. Zheng Y, et al. (2000) Cryo-TEM imaging the flow-induced transition from vesicles to threadlike micelles. *J Phys Chem B* 104:5263–5271.
24. Mendes E, et al. (1997) Shear-induced vesicle to wormlike micelle transition. *J Phys Chem B* 101:2256–2258.
25. Mendes E, Menon SVG (1997) Vesicle to micelle transitions in surfactant mixtures induced by shear. *Chem Phys Lett* 275:477–484.
26. Bernard A, et al. (2005) Shear-induced permeation and fusion of lipid vesicles. *J Colloid Interface Sci* 287:298–306.
27. Sein A, Verheij JA, Agterof WGM (2002) Rheological characterization, crystallization, and gelation behavior of monoglyceride gels. *J Colloid Interface Sci* 249:412–422.
28. Coiro VM, Manigrasso M, Mazza F, Pochetti G (1987) Structure of a triclinic phase of sodium dodecyl sulfate monohydrate. A comparison with other sodium dodecyl sulfate crystal phases. *Acta Crystallogr C* 43:850–854.
29. Palberg T (1999) Crystallization kinetics of repulsive colloidal spheres. *J Phys Condens Matter* 11:R323–R360.
30. Aastuen DJW, Clark NA, Cotter LK, Ackerson BJ (1986) Nucleation and growth of colloidal crystals. *Phys Rev Lett* 57:1733–1737.
31. Besseling TH, et al. (2012) Oscillatory shear-induced 3D crystalline order in colloidal hard-sphere fluids. *Soft Matter* 8:6931–6939.
32. Koppi KA, Tirrell M, Bates FS (1993) Shear-induced isotropic-to-lamellar transition. *Phys Rev Lett* 70(10):1449–1452.
33. Nettesheim F, Zipfel J, Lindner P, Richtering W (2001) Influence of sodium dodecyl sulfate on structure and rheology of aqueous solutions of the nonionic surfactant tetraethyleneglycol-monododecyl ether (C12E4). *Colloids Surf A Physiochem Eng Asp* 183-185:563–575.
34. Shahidzadeh N, Bonn D, Aguerre-Chariol O, Meunier J (1998) Large deformation of giant floppy vesicles in shear flow. *Phys Rev Lett* 81:4268–4271.
35. Safinya CR, Sirota EB, Plano RJ (1991) Nematic to smectic-A phase transition under shear flow: A nonequilibrium synchrotron X-ray study. *Phys Rev Lett* 66(15):1986–1989.
36. Fujii S, Ishii Y, Komura S, Lu CYD (2010) Smectic rheology close to the smectic-nematic transition. *Europhys Lett* 90:64001–64006.
37. Cheng X, Xu X, Rice SA, Dinner AR, Cohen I (2012) Assembly of vorticity-aligned hard-sphere colloidal strings in a simple shear flow. *Proc Natl Acad Sci USA* 109(1):63–67.
38. Bruin S, Jongen ThRG (2003) Food process engineering: The last 25 years and challenges ahead. *Comprehensive Reviews in Food Science and Food Safety* 2:42–81.
39. Chen Y, Lin C, Wu F, Chen H (2009) Rheological properties of crystallized honey prepared by a new type of nuclei. *J Food Process Eng* 32:512–527.
40. Raut JS, Naik VM, Singhal S, Juvekar VA (2008) Soap: The polymorphic genie of hierarchically structured soft condensed-matter products. *Ind Eng Chem Res* 47: 6347–6353.
41. Holme MN, et al. (2012) Shear-stress sensitive lenticular vesicles for targeted drug delivery. *Nat Nanotechnol* 7:536–543.
42. De Silva JP, et al. (2010) RheoSAXS studies of anisotropic complex fluids under shear. *J Phys Conf Ser* 247:012052–012061.